Chapter 6

Plasma diagnostics and models using the improved escape probability

In chapter 2 simple escape probability techniques were applied to C II and C III spectral measurements of the East solar limb using the SOHO-SUMER spectrometer. The line-of-sight averaged escape probability, $\bar{g}\{\tau_0\}$, was used to extract optical depths of certain C II and C III lines from observed branching ratios (see sec. 2.3), from which optical depths of all the lines of these ions can in principle be calculated. The $\bar{g}\{\tau_0\}$ quantity was then coupled with simple stratified atmosphere models to predict intensity ratio variations (figs 2.16a and b). These models were found to be effective from on the disk to beyond the limb at which point the model and observed values began to deviate, possibly indicating the dominance of instrumentally scattered light.

Based on the most effective fit to the observed branching ratios in the C III case, a model limb brightening curve was calculated for the C III $2s2p\,^3P_2$ – $2p^2\,^3P_2$ line at 1175.711 Å (see fig. 2.17). This model was successful on the disk, leading up to the limb but failed in the vicinity of the limb itself. In this region the model fluxes greatly exceeded the observed ones. This discrepancy was echoed in the failure of the escape probability technique to extract optical depth values for the C III lines just beyond the visible limb. The flux model was effective, however, at heights well above the limb where the model ratios failed.

Fits to the ratios were optimised according to optical depth at disk centre, density scale height for the exponential density model, and layer thickness for the constant density model. From the disk centre optical depths obtained, along with those extracted at the limb, the spectral lines of C II and C III were classified according to the effects of opacity on both the population structure and emergent fluxes.

These results demonstrate that the escape probability and absorption factor techniques of chapter 2 provide useful and insightful solutions to the equations of radiative transfer and statistical balance. They also illustrate, however, that they are limited in applicability due to the underlying assumptions upon which they are based. These assumptions relate to variations in the line source functions, atmospheric structure and instrumental effects. Nevertheless, these methods are comparatively simple in comparison with the techniques of radiative transfer and Monte Carlo simulations, and they represent the only means by which optical depths may be extracted from observations in a manner that is model independent. Moreover, the line-of-sight averaged escape probability lends itself naturally to use within arbitrarily complex geometric models of the solar atmosphere.

These facts make the escape probability/absorption factor approach desirable and have prompted the study into their underlying assumptions that is presented here. So far in this study the variation of the source function due to opacity has been analysed and the effects of spectral line blending have been included within the escape probability/absorption factor framework. Furthermore, the influence of atmospheric structure and plasma flow have been considered. These investigations have shown that from consideration of an appropriate stratified, static, plane-parallel atmosphere, an optical depth regime may be identified within which the line-of-sight averaged escape probability, $\bar{g}^{(i)}\{\tau_0\}$, is sufficient to describe the effects of opacity on emergent intensities. It has also been shown that if $\bar{g}^{(i)}\{\tau_0\}$ is valid in the stratified, static case then it is also valid for an atmosphere with structure and non-zero flow providing that the latter does not lead to a deviation of emission profiles from Gaussian.

Figs 6.1a and b show observed line profiles for the C II $2s^22p\,^2P_{3/2} - 2s2p^2\,^2P_{1/2}$ line at 904.481 Å and the C III $2s2p\,^3P_2 - 2p^2\,^3P_1$ line at 1176.370 Å for every pointing

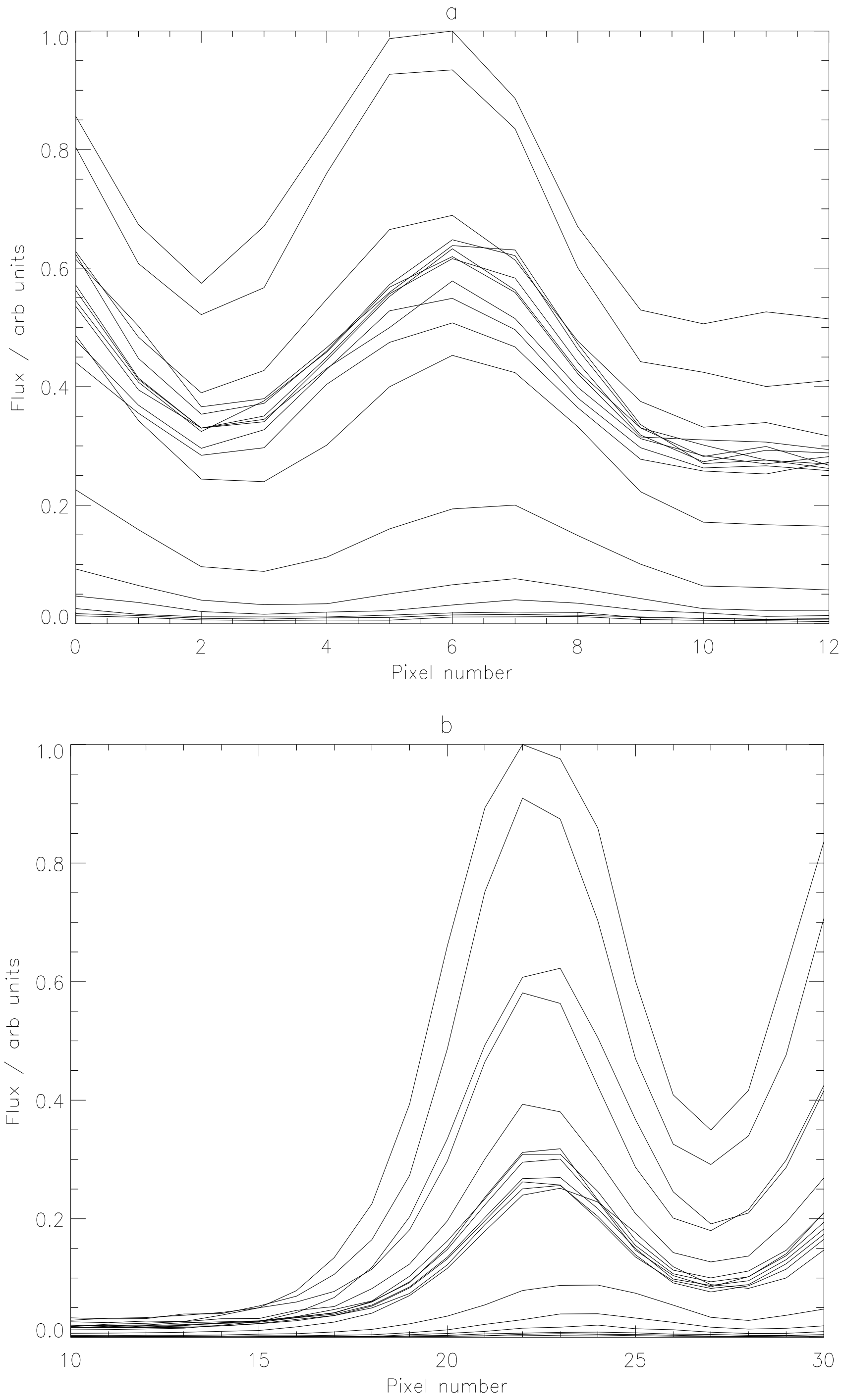

Figure 6.1: Observed line profiles for (a) the C II $2s^2 2p\,^2P_{3/2} - 2s2p^2\,^2P_{1/2}$ line at 904.481 Å and (b) the C III $2s2p\,^3P_2 - 2p^2\,^3P_1$ line at 1176.370 Å. Profiles are shown for every pointing position.

position. These lines are unblended yet display no significant deviation from Gaussian at any point. It follows that for both the C II and C III datasets considered here, plasma flow may be included implicitly. Furthermore the disk centre optical depths deduced in chapter 2 imply that the $\bar{g}^{(i)}\{\tau_0\}$ expression is valid for the spectral lines of both these ions regardless of the structuring of the atmosphere.

In this chapter the SOHO-SUMER data discussed in chapter 2 is re-assessed using the blended escape probability from both a diagnostic and modelling perspective. The analyses so far, coupled with consistent treatment of the variation of optical depth with line-of-sight and the inclusion of instrumentally scattered light, allow the discrepancies found in chapter 2 between modelled and observed quantities to be resolved. In the process, the neglect of the spatial variation of the source function due to the variation of (T_e, N_e) will be justified. Additionally, spicule-like structures that are unresolved by the SUMER spectrometer will be identified.

6.1 The geometric extension of the line-of-sight

In chapter 2 the escape probabilities were derived within a constant density framework but were considered in variable density models. It has subsequently been shown that providing the source function is constant the $g^{(i)}\{\tau_0\}$ and $\bar{g}^{(i)}\{\tau_0\}$ expressions remain the same in the variable density case. However, the definition of τ_0 does change. In the constant density case the optical depth is given by

$$\tau_0 = \kappa_0 N_l \int_{l.o.s.} ds = \kappa_0 N_l L \tag{6.1}$$

where L is the length of the line-of-sight. In this case the geometric extension of the line-of-sight as a whole controls the variation of the optical depth with pointing position. In the variable density case, however, the optical depth is given instead by

$$\tau_0 = \kappa_0 \int_{l.o.s.} N_l(s) ds \tag{6.2}$$

For a stratified model it is again the geometric extension of the line-of-sight that controls the variation of optical depth, but due to the curvature of the atmosphere each *sub-layer* extends differently. Take, for example, the line-of-sight corresponding to the inner edge of the emitting layer (approximately 962 arc sec). This line-of-sight intersects the inner edge of the emitting layer tangentially, but emerges from the layer at a sharper angle. Therefore the sub-layers near the inner edge of the emitting layer are extended to a greater extent in this region than those near the outer edge. This leads to a stronger disk-to-limb variation of optical depth in the models where the density of the emitting layer decreases with height.

Fig. 6.2a shows observed and model limb-brightening curves for the C III $2s2p\,^3P_2 - 2p^2\,^3P_2$ line at 1175.711 Å. Model values are shown including and excluding line blending. The dotted line is directly comparable with fig. 2.17 from which it can be seen that the correct evaluation of optical depth has a marked influence upon the calculated fluxes. The fit is improved in the vicinity of the limb, although a discrepancy remains. Beyond the limb the fall-off of intensity is less well tracked than before.

Fig. 6.2b shows the corresponding branching ratios, I(2–2)/I(1–2), which are comparable with those of fig. 2.16b. Certain features are as expected: line blending leads to an increase in effective optical depth and improves the fit as compared with the unblended case and the optimal optical depth is less in the blended case. However, given, as stated above, that the optical depth variation in the variable density case is more marked than in the constant density case, it is somewhat surprising that the model curves to not track the observed ones so well as in fig. 2.16b. The reason for this is that the expression for optical depth used in chapter 2 ($\tau_0 = const \times \delta / \cos\theta$) is an approximation and breaks down, becoming infinite, at the inner edge of the emitting layer. Thus with this expression the optical depths are overestimated in the vicinity of the limb and this serves, ironically, to improve the fit to the ratios. It is also responsible, however, for the extent of the overestimate of the fluxes at the limb observable in fig. 2.11.

There remains a discrepancy between the observed and model fluxes and ratios in the region of and beyond the limb. The model overestimates both the fluxes and ratios in the vicinity of the limb, whereas beyond this region the fluxes are underestimated and the ratios are overestimated. The situation at the limb is interesting since if it is assumed that the ratio of upper to lower level population density is constant throughout the layer (i.e. that $\bar{g}^{(i)}\{\tau_0\}$ is valid) then fig. 6.2a implies that the column

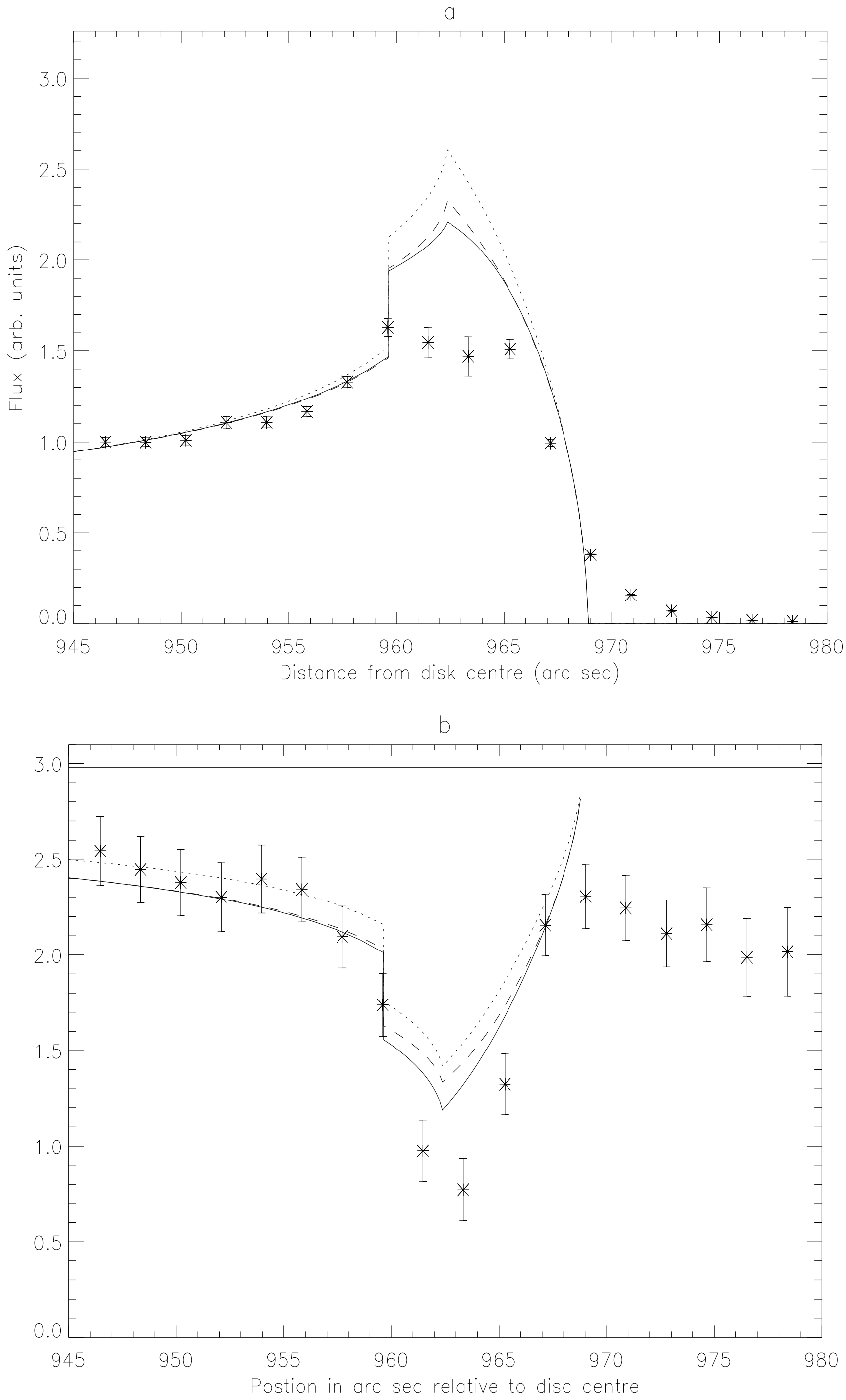

Figure 6.2: (a) Observed fluxes versus raster position for the C III $2s2p^3P_2$ – $2p^{2\,3}P_2$ line at 1175.711 Å. The solid line represents $\bar{g}^{(i)}\{\tau_0\}$ based model results with blending included (eq. 4.5) and with a disk centre optical depth of 0.16. The dotted line represents the same but with blending excluded (eq. 2.17). The dashed line represents the unblended calculation with an optical depth of 0.2. (b) Observed branching line intensity ratios versus raster position in arc sec relative to the disk centre for the C III I(2–2)/I(1–2) ratio as in fig. 2.15b. Solid, dotted and dashed lines are as in (a).

density is overestimated by the model, and fig. 6.2b implies the opposite. This paradox suggests the presence of structures that are observationally unresolved. This will be discussed later.

6.2 Instrumentally scattered light

In chapter 2 it was speculated that the off-limb discrepancy between the model and observed branching ratios indicated the dominance of instrumentally scattered light. If so then it is possible that scattered light will also account for the discrepancy in the fluxes at such heights. It is expected that the branching ratios should return to their optically thin values well above the limb as the (apparent) density of the atmosphere decreases. For C III this is not found. Rather the ratios in this case move closer to their on-disk values at heights above $\sim$ 970 arc sec. This is true even though the fluxes at these heights are very much smaller than those on disk. In addition, Doppler shifts of multiplet lines to the blue, seemingly indicative of tangential flows of the order of 20 km/s, are seen in the C III lines. The region of apparent onset of these shifts is the same as that where the branching ratios begin to deviate from the model values. These facts suggest that at heights above $\sim$ 970 arc sec instrumentally scattered light – that which originates from all locations on the sun and scatters off the interior of the telescope prior to passing through the entrance slit – dominates the observed signal. If this is so then the observed Doppler shifts indicated upflows on-disk and not beyond the limb.

The entire disk contributes to the scattered light signal with the contribution from each point being characterised by the instrument point spread function, *psf*, which represents the relative intensity of a point source as a function of lateral distance from the slit. This is shown in fig. 6.3. David et al. (1997) have shown that the pre-launch point spread function is still effective and so it may be used to complete the calculation. The emitted flux, $\mathcal{F}$, from position $\mathbf{h}$, which is related to the emitted intensity via $\mathcal{F}(\mathbf{h}) = const \times I(\mathbf{h})$, is given by

$$\mathcal{F}(\mathbf{h}) = \int\int_{disk} \mathcal{F}_t(\mathbf{x}) \times psf(|\mathbf{h}-\mathbf{x}|)d\mathbf{x} \tag{6.3}$$

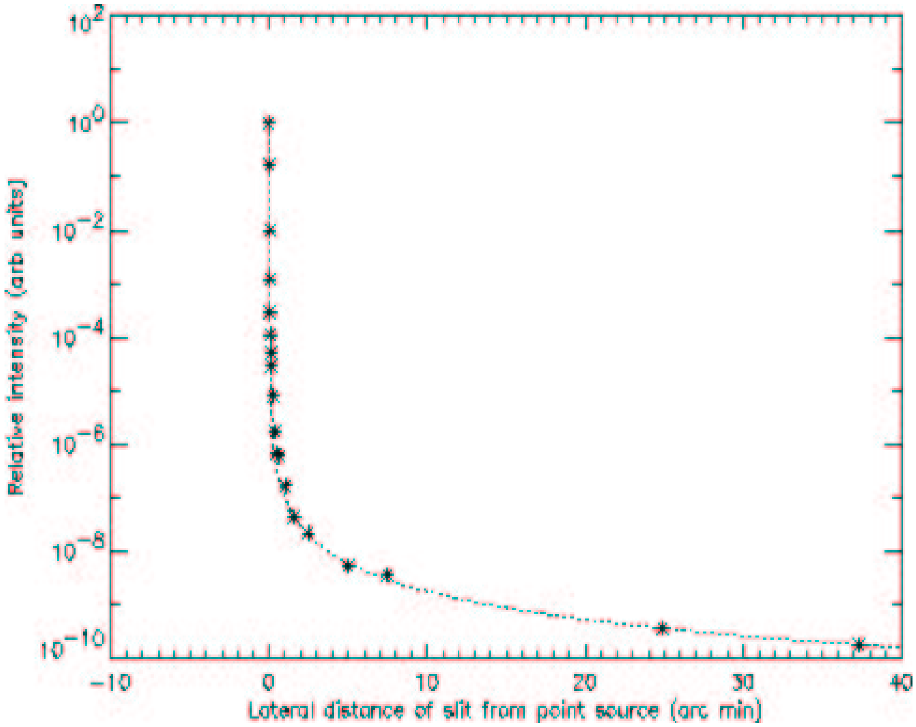

Figure 6.3: The SUMER pre-launch point spread function ($*$'s) (Lemaire, 1998) – relative intensity of a point source versus lateral distance from source to slit centre. The dotted line is a fit to the measured points used in the analysis described.

where $\mathcal{F}_t(\mathbf{x})$ is the true signal. Scattered light may be included within all the models presented so far using eq. 6.3. Model fluxes and ratios including the effects of instrumentally scattered light are presented below.

6.3 Model predictions

The three atmosphere models presented in chapter 2 are considered again. A fourth model is introduced that is a composite of models 1 and 3, comprising of a narrow TR shell with an exponential component to account for the extension of the TR into the corona due to spicule-like structures. Thus the models may be summarised as

1. Thin TR based on the VAL atmosphere model

2. Spherical shell of constant density
3. Layer of density that falls off exponentially with height
4. Composite of models 1 and 3

Each of these models includes the effects of line blending and scattered light. Using these stratified atmosphere models, limb-brightening curves and branching ratios versus pointing position may be calculated using eqs 3.25 and 4.5. Since it is assumed that the source function is constant in space, eq. 3.25 is equivalent to eq. 2.43, which was used in chapter 2 to model limb-brightening curves.

6.3.1 Fluxes

The observed spectral line fluxes for the C II $2s^22p\ ^2P_{3/2} - 2s2p^2\ ^2S_{1/2}$ line at 1037.020 Å and the C III $2s2p\ ^3P_2 - 2p^2\ ^3P_2$ line at 1175.711 Å are shown in figs 6.4a and b respectively with the predicted fluxes (calculated via eq. 3.25) overlaid. Model 1 fails completely for both C II and C III as expected since it does not recognise the extension of the TR into the corona due to spicules and other structures. For this model, all the emission above 962 arc sec is due to scattered light. Also the point of peak emission in this model is shifted back from 962 arc sec to $\sim$ 960.5 arc sec since at this height there is a scattered light contribution from positions closer to and further from the solar disk. In contrast, at 962 arc sec there are only contributions to the scattered light component are from positions nearer to disk centre. Models 2, 3 and 4 track the trend in both cases in broad terms but not in detail, failing most markedly at the limb and well off limb. On disk, despite the averaging over the slit, the fluxes display a sensitivity to the structural detail. This detail is evident in the surface plots in figs 2.8a and b. The sensitivity of the emergent flux to column density is implied by eq. 3.25 since $\bar{g}\{\tau_0\}$ is insensitive to optical depth for values greater than ~ 1 (see fig. 2.2).

At heights of $\sim$ 970 arc sec and above, despite the inclusion of scattered light, the fluxes are not tracked well by the models. Rather, the models predict intensities significantly smaller than those observed.

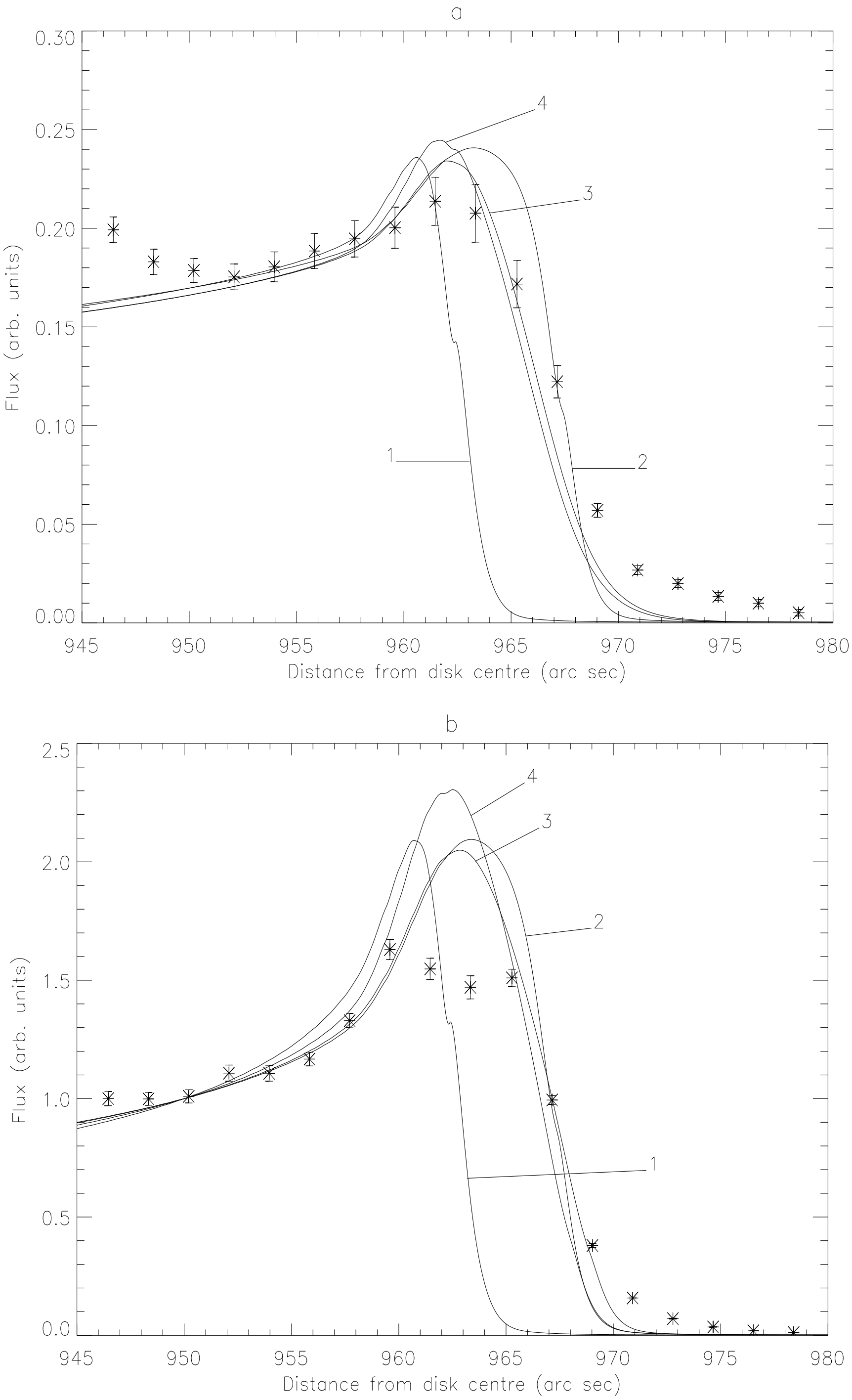

Figure 6.4: Observed and model fluxes for the (a) C II $2s^22p\ ^2P_{3/2} - 2s2p^2\ ^2S_{1/2}$ line at 1037.020 Å and (b) the C III $2s2p\ ^3P_2 - 2p^2\ ^3P_2$ line at 1175.711 Å. The $*$'s correspond to the observed fluxes and the solid lines are the model predictions numbered as in the text. Note that the visible limb is at 959.6 arc sec.

The inclusion of line blending, scattered light and the improved calculation of optical depth for each line-of-sight has a marked influence on the predicted fluxes. This difference is evident in the comparison of fig. 6.4b with fig. 2.17. It can be seen that these advancements to the models improve the fit to the fluxes at the limb but at heights beyond the limb the fit is less effective than before. Furthermore, while the fit is improved at the limb, the fluxes are still significantly overestimated by the models.

6.3.2 Ratios

The observed and model flux ratios of the (3/2–1/2)/(1/2–1/2) components of the C II $2s^22p\ ^2P - 2s2p^2\ ^2S$ multiplet and the (2–2)/(1–2) components of the C III $2s2p\ ^3P - 2p^2\ ^3P$ multiplet are shown in fig 6.5a and b respectively. The models here are much more effective than in the case of emergent fluxes since the linear dependence of the intensity on column density (eq. 3.25) is factored out (eq. 2.22). In the C III case the dip in the ratios at the limb is underestimated yet optical depths at this point are such that the $\bar{g}^{(i)}\{\tau_0\}$ ratio, in the absence of blending, is insensitive to optical depth (see fig. 6.6). When blending is included, absorption of 2–2 line photons by the 1–1 line leads to a decrease in the ratio. The underestimation of the observed values by the model at the limb suggests an underestimate in lower level population density of either the 2–2 line or the 1–1 line yet at this point the emergent intensities are overestimated suggesting an overestimate in the upper level column densities. This discrepancy is possibly due to a structure, not along the line-of-sight but along the slit. This will be discussed further in sec. 6.7.

For the model branching ratios the inclusions of scattered light is sufficient to ensure agreement within the error bars to the observed values at heights of $\sim$ 970 arc sec and above. Comparison of figs 6.5a and b with figs 2.16a and b shows that the more advanced methods used here lead to an improvement to the fit to the ratios beyond the limb but a worse fit at the limb. Curiously the improvement in the fit to the ratios occurs where the fit to the fluxes reduces in quality, and vice versa.

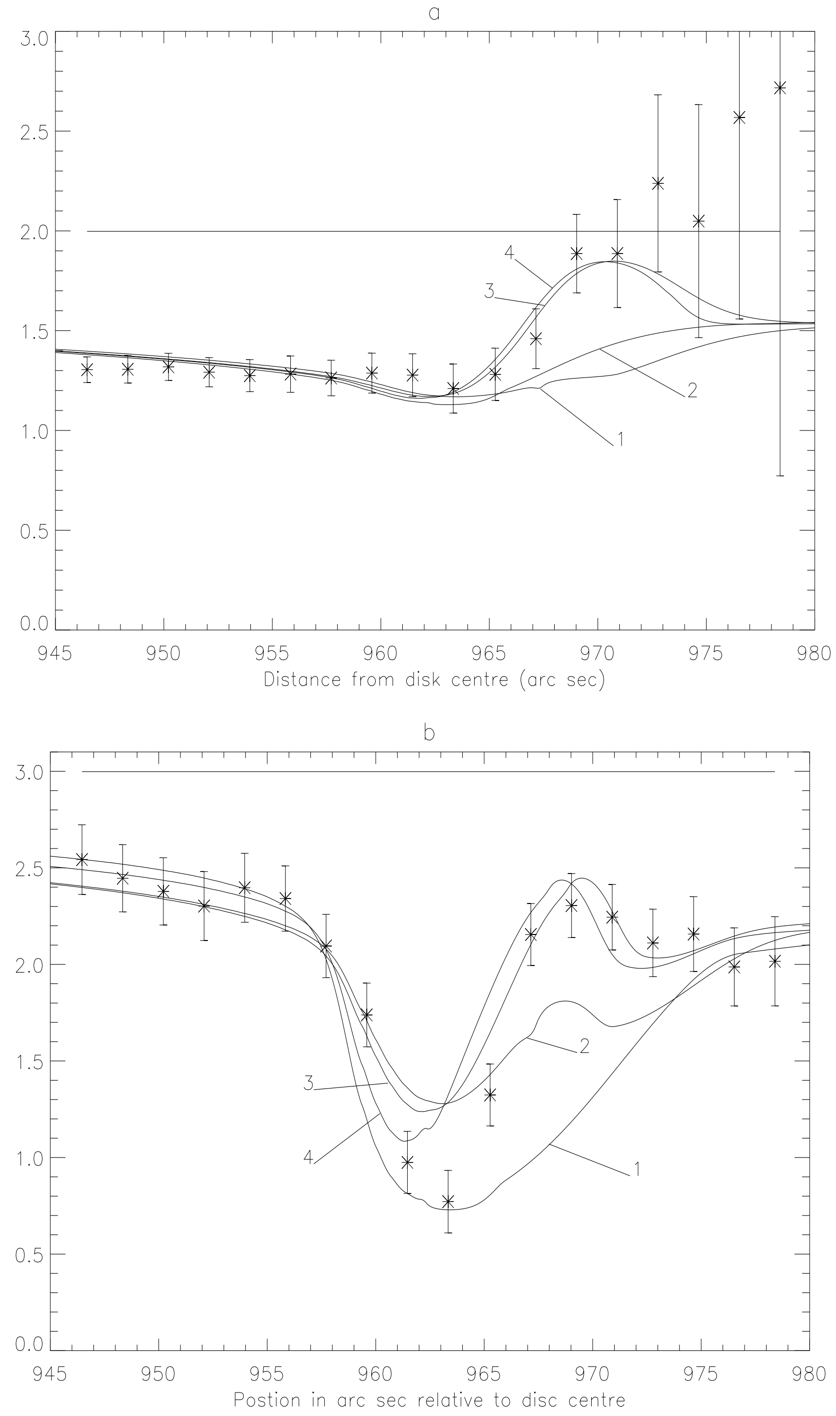

Figure 6.5: Observed and model branching ratios of the (a) (3/2–1/2)/(1/2–1/2) components of the C II $2s^22p\ ^2P$ – $2s2p^2\ ^2S$ multiplet and (b) the (2–2)/(1–2) components of the C III $2s2p\ ^3P$ – $2p^2\ ^3P$ multiplet.

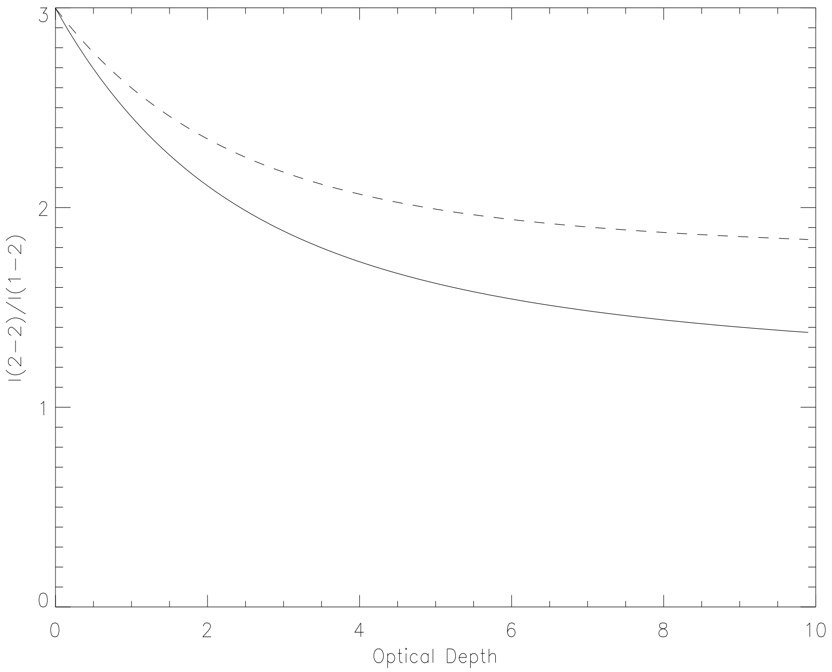

Figure 6.6: Intensity ratio of C III (2–2)/(1–2) versus optical depth for the unblended (dashed) and blended (solid) cases, calculated using eqs 2.17 and 4.5 respectively.

6.3.3 Discussion

The best fit to the observed ratios for each model yields optimal parameters for each of the two ions. The two most effective models in each case are models 3 and 4 for which the most significant parameters are optical depth at disk centre and density scale height. The disk centre optical depths returned were 0.7 and 0.15 for the C II $2s^2 2p\,^2P_{3/2} - 2s2p^2\,^2S_{1/2}$ line at 1037.012 Å and the C III $2s2p\,^3P_2 - 2p^2\,^3P_2$ line at 1175.711 Å respectively. These compare with values obtained in chapter 2 of 0.6 and 0.16 respectively. The difference in the C II case is due to the improved calculation of optical depth whereas the difference in the C III case is principally due to the inclusion of line blending.

Optimisation of density scale height yields values of 1.2 and 2.5 arc sec for both models 3 and 4 for C II and C III respectively. The scattered light signal becomes significant at heights beyond the inner edge of the emitting layer – i.e. as the (apparent) density falls off to zero. As a consequence the optimised scale height is dependent upon the inclusion of scattered light. Specifically, it is less when scattered light is included. When it is excluded the optimal scale height for C III is 4 arc sec. These compare with values obtained in chapter 2 of 1.3 and 1.4 arc sec respectively. The difference in the C II values is due to the inclusion of scattered light. The difference in the C III case is due to the inaccurate fit to the observed ratios at the limb.

Fig. 6.5b shows that model 4 is slightly more effective than model 3 in describing the C III ratio variation across the limb. However, the relative magnitude of model 1 to model 3 in the composite case was treated as an adjustable parameter and while a large value (~ 100) is optimal in the C III case, a low value, namely 0, is the optimal value for C II. As a consequence model 4 is considered in this study to be largely redundant. The scale heights in both cases are similar to the ~ 1.5 arc sec findings of Mariska et al. (1978) and to those found in chapter 2 – noting that the C III scale height is likely to be an over estimate as the slope of the ratios in the region from $964 \rightarrow 970$ arc sec is not matched. They also agree with both in terms of the decrease with decreasing temperature of line formation.

In order for the scattered light to dominate at the appropriate point in the C III data, a departure from the exponential fall off of density is required. A cut-off is introduced in the model for this purpose, the position of which may be optimised for agreement with the observed ratios. This cut-off is found to be at ~ 969 arc sec. This value is influenced by the fact that the scale height is optimised as described above and is thus overestimated. Consequently in the absence of a cut-off the predicted onset of scattered light occurs later than observed.

A possible interpretation for this departure from an exponential fall off, or at least a change or even discontinuity in scale height, follows from the model considered by Mariska et al. (1978) who, as stated in chapter 2, envisaged cylindrical spicules. The exponential fall off of density in this picture reflects the change in filling factor as the number of spicules intersected by the line-of-sight decreases with distance beyond the limb. Ultimately, however, the density variation will reflect the genuine density variation at the top of a spicule. However, the introduction of this parameter is introduced so that the off-limb discrepancy between observed and model branching ratios (seen in figs 2.16 and 6.2b) might be resolved by the inclusion of scattered light. This it does, but it does not account for the emergent fluxes observed at such heights. It is therefore likely that this parameter is a numerical fudge.

As predicted in chapter 2, the inclusion of scattered light is sufficient to match the off-limb model C III branching ratios to the observed ones within the error bars. However, the discrepancy between the model and observed fluxes at heights beyond $\sim$ 970 arc sec is non-trivial. This suggests that the signals at such heights are true and not dominated by instrumentally scattered light. If so, then the branching ratios indicate that the optical depths at heights beyond $\sim$ 970 arc sec are comparable with those on disk which in turn imply comparable column densities. The fluxes at such heights, however, are significantly smaller than those on disk which indicate that the column densities are significantly smaller than the ones on the disk. This is a paradox which may be resolved if the emitting structures at heights beyond $\sim$ 970 arc sec are unresolved (see sec. 6.7).

6.4 Comments on the effectiveness of stratified models

It is clear that stratified models are sufficient to track the branching ratio variations well, failing only in the C III case in the vicinity of the inner edge of the emitting layer. Furthermore, the inclusion of scattered light leads to an effective fit to the ratios above heights of $\sim$ 970 arc sec where previously there was a discrepancy between the model (and intuitive expectations) and the observations. The fit to the emergent fluxes, on the other hand, is improved compared to that in sec. 2.7, but, nevertheless, still not modelled well. Moreover, in the case of the fluxes, scattered light is not sufficient to explain the signals off limb. It is natural to conclude that this is due to the failure of the stratified model at heights lower than the region of scattered light dominance. But even if the observed signal is used to calculate the scattered contribution, the predicted signal at heights above ~ 970 arc sec is still much lower than that observed.

If the signal in these regions is predominantly a true signal, the issue of the mismatch between the column densities at such heights implied by the branching ratios, and those implied by fluxes resurfaces. In addition, the interpretation of the Doppler shifts discussed in sec 2.4 is again in doubt. The signals, being true, imply that these shifts indicate either 20 km/s upflows beyond the limb or 20 km/s downflows on disk, and at the limb. As discussed in chapter 1, although both upflows and downflows are evident in TR spectral lines, spectral emission from downflowing plasma is dominant. Typical velocities are $\sim 5 \rightarrow 16$ km/s (Brekke et al., 1997) which are less than those found here. They are, however, consistent in magnitude with velocities associated with rising spicule structures (Lorrain & Koutchmy, 1996). If the shifts are to the red, then they persist up until the limb. This is inconsistent with the analyses of Athay & Dere (1989) and Henze & Engvold (1992) who found that the shifts vanished at the limb. Feldman et al. (1982), however, suggest that the redshifts do not disappear at the limb though they do decrease. Following this, the findings here would suggest downflows of velocity greater than 20 km/s on disk.

As discussed earlier, the relative effectiveness of the fit to the ratios as compared with the fluxes is due to the fact that the linear dependence of the fluxes on column density is factored out in the ratios. This dependence is present in the fluxes themselves. Thus the ratios are relatively insensitive to structure. Since the ratios are indicators of absorption which is characterised by the absorption factor, this insensitivity to structure illustrates the appropriateness of the stratified model in the calculation of the absorption factor. This also follows intuitively from eq. 2.33 in which the intensity term is integrated over volume, thus averaging over the structural detail.

The fits to the fluxes, however, demonstrate a sensitivity to structure. The stratified models are able to describe the emission in broad terms but not in detail. For a more accurate fit, the fine structure must be included in the emergent flux model.

Table 6.1: Summary of data for the C III $2s2p\ ^3P_2 - 2p^2\ ^3P_2$ transition for each raster scan position. $\tau_{0,2-2}/\tau_{0,1-2} = 3.204$

Pos.(")	$\tau_{0,2-2}$	$\bar{g}\{\tau_{0,2-2}\}$	Pos.(")	$\tau_{0,2-2}$	$\bar{g}\{\tau_{0,2-2}\}$
943.06	0.61 (0.74)	0.80 (0.78)	959.94	54.0 (-)	0.03 (-)
944.94	0.80 (0.94)	0.75 (0.74)	961.88	5.40 (8.64)	0.27 (0.21)
946.81	0.90 (1.09)	0.73 (0.71)	963.75	1.40 (1.68)	0.62 (0.60)
948.69	1.05 (1.27)	0.69 (0.67)	965.63	1.04 (1.27)	0.70 (0.67)
950.56	0.86 (1.05)	0.74 (0.71)	967.50	1.20 (1.42)	0.66 (0.64)
952.44	1.00 (1.18)	0.71 (0.69)	969.38	1.50 (1.81)	0.61 (0.58)
954.31	1.51 (1.86)	0.60 (0.58)	971.25	1.40 (1.67)	0.62 (0.60)
956.19	2.70 (3.42)	0.45 (0.41)	973.13	1.81 (2.24)	0.56 (0.53)
958.06	15.0 (-)	0.11 (-)	975.00	1.72 (2.13)	0.57 (0.54)

6.5 Extraction of optical depth from observations and the validity of the escape probability approach

Optical depths may be deduced from the branching ratios with blending included following the approach described in sec. 2.3. Results corresponding to those of tables 2.1, 2.3 and 2.5 are shown in tables 6.1 → 6.3. The values in brackets are those deduced without blending (i.e. those of tables 2.1, 2.3 and 2.5). It can be seen that in each case the optical depths deduced when blending is included are smaller than those obtained when it is not.

It is interesting to note that for the C III $2s2p\ ^3P_2$ – $2p^2\ ^3P_2$ transition (table 6.1) the blended $\bar{g}^{(i)}\{\tau_0\}$ is effective in extracting optical depth values at 958.06 and 959.94 arc sec. With and without blending the $\bar{g}\{\tau_0^{(1)}\}/\bar{g}\{\tau_0^{(2)}\}$ curves decrease monotonically with a gradient that also decreases with optical depth (see fig. 6.6). Furthermore the gradient is greater when blending is included. Consequently, while without blending the $\bar{g}\{\tau_0\}$ quantity yields unphysical optical depths at 958.06 and 959.94 arc sec the values are meaningful when blending is included.

Table 6.2: Summary of data for the C II $2s^22p\ ^2P_{3/2} - 2s2p^2\ ^2S_{1/2}$ transition for each raster scan position. $\tau_{0,3/2-1/2}/\tau_{0,1/2-1/2} = 1.97$. These values are the same as in table 2.3 since there is no line blending here.

Pos.(")	$\tau_{0,3/2-1/2}$	$\bar{g}\{\tau_{0,3/2-1/2}\}$	Pos.(")	$\tau_{0,3/2-1/2}$	$\bar{g}\{\tau_{0,3/2-1/2}\}$
943.06	5.30 (5.30)	0.31 (0.31)	959.94	10.2 (10.2)	0.18 (0.18)
944.94	5.25 (5.25)	0.31 (0.31)	961.88	6.00 (6.00)	0.28 (0.28)
946.81	4.95 (4.95)	0.32 (0.32)	963.75	2.82 (2.82)	0.46 (0.46)
948.69	5.70 (5.70)	0.29 (0.29)	965.63	0.36 (0.36)	0.88 (0.88)
950.56	6.23 (6.23)	0.27 (0.27)	967.50	0.36 (0.36)	0.88 (0.88)
952.44	6.00 (6.00)	0.28 (0.28)	969.38	- (-)	- (-)
954.31	6.70 (6.70)	0.26 (0.26)	971.25	- (-)	- (-)
956.19	5.80 (5.80)	0.29 (0.29)	973.13	- (-)	- (-)
958.06	6.20 (6.20)	0.27 (0.27)	975.00	- (-)	- (-)

Table 6.3: Summary of data for the C II $2s^22p\ ^2P_{3/2} - 2s2p^2\ ^2P_{3/2}$ transition for each raster scan position. $\tau_{0,3/2-3/2}/\tau_{0,1/2-3/2} = 5.05$.

Pos.(")	$\tau_{0,3/2-3/2}$	$\bar{g}\{\tau_{0,3/2-3/2}\}$	Pos.(")	$\tau_{0,3/2-3/2}$	$\bar{g}\{\tau_{03/2-3/2}\}$
943.06	3.20 (4.95)	0.39 (0.32)	959.94	3.05 (4.69)	0.40 (0.33)
944.94	3.23 (5.01)	0.39 (0.32)	961.88	3.13 (4.84)	0.40 (0.33)
946.81	2.71 (4.13)	0.43 (0.36)	963.75	2.90 (4.40)	0.42 (0.35)
948.69	2.86 (4.37)	0.42 (0.35)	965.63	1.90 (2.88)	0.53 (0.46)
950.56	3.31 (5.15)	0.38 (0.31)	967.50	1.54 (2.36)	0.59 (0.51)
952.44	3.12 (4.81)	0.40 (0.33)	969.38	0.58 (1.07)	0.81 (0.71)
954.31	3.00 (4.56)	0.41 (0.34)	971.25	0.83 (1.40)	0.74 (0.65)
956.19	3.40 (5.23)	0.37 (0.31)	973.13	1.01 (1.63)	0.70 (0.61)
958.06	3.30 (5.10)	0.38 (0.31)	975.00	0.75 (1.29)	0.76 (0.67)

6.6 Removing the discrepancy between model and observed spectral data

It is clear that the stratified models presented, in conjunction with the blended, line-of-sight averaged escape probability, $\bar{g}^{(i)}\{\tau_0\}$, are unable to accurately describe the C II and C III spectral characteristics observed by SOHO-SUMER in the vicinity of the solar limb. Yet it has been asserted in this work that $\bar{g}^{(i)}\{\tau_0\}$ is appropriate and accurate in describing the effects of opacity in the spectral lines of these ions. If this is true then the failure of the models presented is in their treatment of structure, and thus the variations in column density, and *not* due to a dependence of the source function on space or frequency either due to photon scattering or plasma flow. To demonstrate that this is the case, consider fig. 6.7. This shows observed fluxes for the C III $2s2p\ ^3P_2 - 2p^2\ ^3P_2$ line at 1175.711 Å with the function $\tau_0 \bar{g}^{(i)}\{\tau_0\}$ overlaid. Here the optical depth at each point is not based on any model, stratified or otherwise. Rather the optical depths are those extracted from the observed ratios and listed in table 6.1. The predicted fluxes are scaled to match the observed value at 943.06 arc sec. The discrepancy is marked and denotes a failure in the escape probability model. Clearly at least one assumption underpinning the theory is not valid.

It has been shown that the modification to the source function due to opacity is not significant for either the C II or C III. However, it was shown in chapter 3 that there is a spatial variation of the source function due to the variation of electron density and temperature through the emitting layer. This variation was overlooked and the assumption was made that each emitting layer may be represented by a single (T_e, N_e) pair. This assumption was motivated by the notion of an emitting layer comprising of thin TR sheaths surrounding spicule-like structures which extend into the corona with lengths greatly exceeding the thickness of each sheath. This assumption allowed the modification to the source function purely due to opacity – or alternatively, scattering into the line-of-sight – to be considered. It was not justified at the time and thus it is conceivable that this variation is partially or wholly responsible for the breakdown of the $\tau_0 \bar{g}^{(i)}\{\tau_0\}$ expression evident in fig. 6.7.

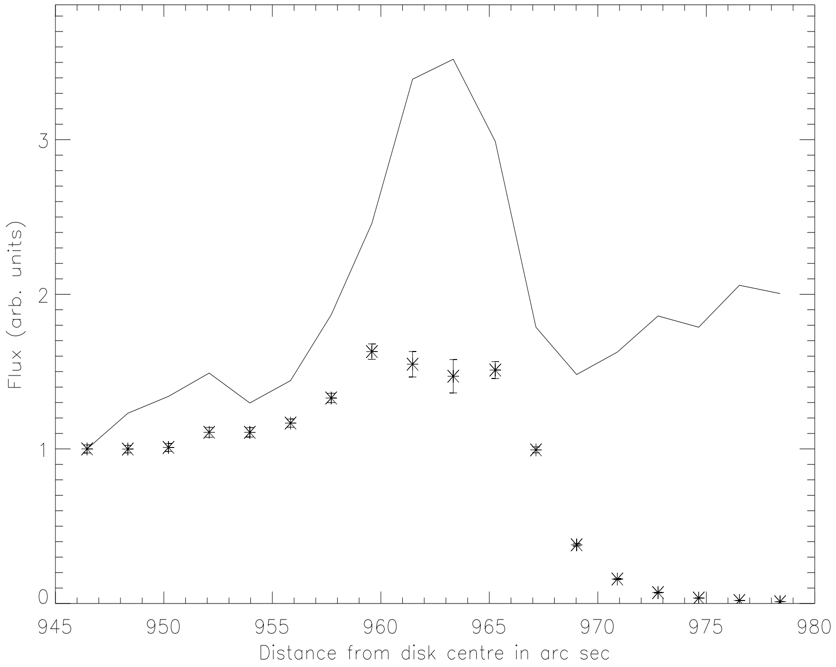

Figure 6.7: Observed fluxes for the C III $2s2p\ ^3P_2 - 2p^2\ ^3P_2$ line at 1175.711 Å. Overlaid is the function $\tau_0 \bar{g}^{(i)}\{\tau_0\}$ (solid line) where the optical depths, τ_0, for each position are taken from table 6.1.

It was shown in sec. 3.10 that the intensity of an unblended line may be written as

$$I \quad \sim \quad \bar{N}_l \bar{g}\{\tau_0\} L f_{los}\{\tau_0\} \tag{6.4}$$

where

$$f_{los}\{\tau_0\} = \int_0^L \frac{\tilde{N}_u(t)}{\tilde{N}_l(t)} \frac{g(t)}{\bar{g}\{\tau_0\}} dt \tag{6.5}$$

This extends to blended lines if $\bar{g}^{(i)}\{\tau_0\}$ replaces $\bar{g}\{\tau_0\}$ in eq. 6.4. There is therefore a key issue relating to the nature of the dependence of $f_{los}\{\tau_0\}$ on line-of-sight and optical depth.

Within the picture of thin sheaths around extended spicule-like structures, the line-of-sight optical depth is principally determined by the number of structures intersected by that line-of-sight. Providing the conditions within each sheath are similar, the dependence of $f_{los}\{\tau_0\}$ on line-of-sight will be weak. The optical depth is smaller on-disk than at the limb – for example the model based optical depth at disk centre for the C III $2s2p\ ^3P_2 - 2p^2\ ^3P_2$ line at 1175.711 Å is 0.16 which compares with observationally deduced values of 0.61 and 1.40 at 943.06 and 963.75 arc sec respectively. Thus it may be deduced that for C II and C III optical depth of a single sheath is small and that the number of structures intersected by the each line-of-sight in the vicinity of the limb is large.

If the variation of the source function with respect to space is responsible for the deviation of observed and predicted fluxes in fig. 6.7, a correlation between this deviation and optical depth is expected. This would manifest itself at each raster position in a line to line variation of the deviation. An investigation into this is presented below but first, consider the dependence of the source function on frequency.

It has been shown in chapters 4 and 5 that the possible contributors to a dependence of the source function on frequency are either negligible or manageable within the escape probability framework. The relevant optical depths are sufficiently small that scattering into the line-of-sight is insignificant. Consequently the effects of blending may be included within the line-of-sight averaged escape probability, $\bar{g}^{(i)}\{\tau_0\}$. They are also sufficiently small to ensure complete frequency redistribution. This is confirmed by the observed line profiles which suffer minimal deviations from Gaussian profiles which may be described within the escape probability theory. Also confirmed by the observed profiles is the fact that plasma flow, though evident from the observed Doppler shifts (see sec. 2.4), presents no difficulty and may be accounted for within the blending formulation. Photon scattering can lead to a dependence of the source function on frequency through partial frequency redistribution. Multiple scattering in the wings of the Lα line of hydrogen can lead to significant changes in the flux of that line which in turn can affect the charge balance and gas pressure through modification of the ionisation balance of hydrogen. However, the effects of partial frequency redistribution on line fluxes of other lines are not typically very large and so complete frequency redistribution is usually a good approximation (Hubeny &

Lites, 1995). This is confirmed by fig. 6.1 which shows no significant deviation from Gaussian profiles.

The third potential source for the deviation of predicted from observed fluxes is atmospheric structure. In chapter 5 structure was discussed and it was demonstrated that it leads to a reduction in the degree of absorption within a plasma. Therefore, if the validity of $\bar{g}^{(i)}\{\tau_0\}$ is confirmed by consideration of the absorption factor within a stratified atmosphere model, then the presence of structure will strengthen rather than threaten this validity. Hence, from the perspective of the modification to the population structure (or scattering into the line-of-sight), structure does not influence the validity of the $\bar{g}^{(i)}\{\tau_0\}$ expression. Moreover, it was demonstrated in chapter 3 (see sec. 3.3) that if it is assumed that the source function is constant in space, then the $\bar{g}^{(i)}\{\tau_0\}$ expression is independent of the nature of the variation of density along the line-of-sight. So structure along the line-of-sight is not responsible for the discrepancy in fig. 6.7. However, structure will influence the fluxes if the observed structures are smaller in one or more dimension than the resolution limit of the instrument – i.e. if the observed structures are unresolved. If this is so then the term $f_{los}\{\tau_0\}$ may be interpreted as a *filling factor*. This is a purely geometric quantity and is therefore independent of optical depth.

If structure is responsible for the discrepancy in fig. 6.7, then in contrast to the case of the source function variation being responsible, a constancy of $f_{los}\{\tau_0\}$ with respect to τ_0 is expected.

Shown in fig. 6.8 are observed fluxes versus raster position for each component of the C III $2s2p\ ^3P$ – $2p^2\ ^3P$ multiplet with plots of $f_{los}\{\tau_0\}\tau_0\bar{g}^{(i)}\{\tau_0\}$ overlaid. As in fig. 6.7, the optical depths are those listed in table 6.1. The factors $f_{los}\{\tau_0\}$ are determined such that the observed and predicted fluxes in fig. 6.7 match exactly and so for each raster position there is only one scaling factor for all the lines of the multiplet. It can be seen from this figure that the single set of factors $f_{los}\{\tau_0\}$ is sufficient to match the predicted intensities to the observed ones almost exactly for each line with the exception of the 1–1 and 1–0 components. Both these are blended and the discrepancy between predicted and observed values is most significant in the vicinity of the limb which corresponds to the region of most significant optical thickness and

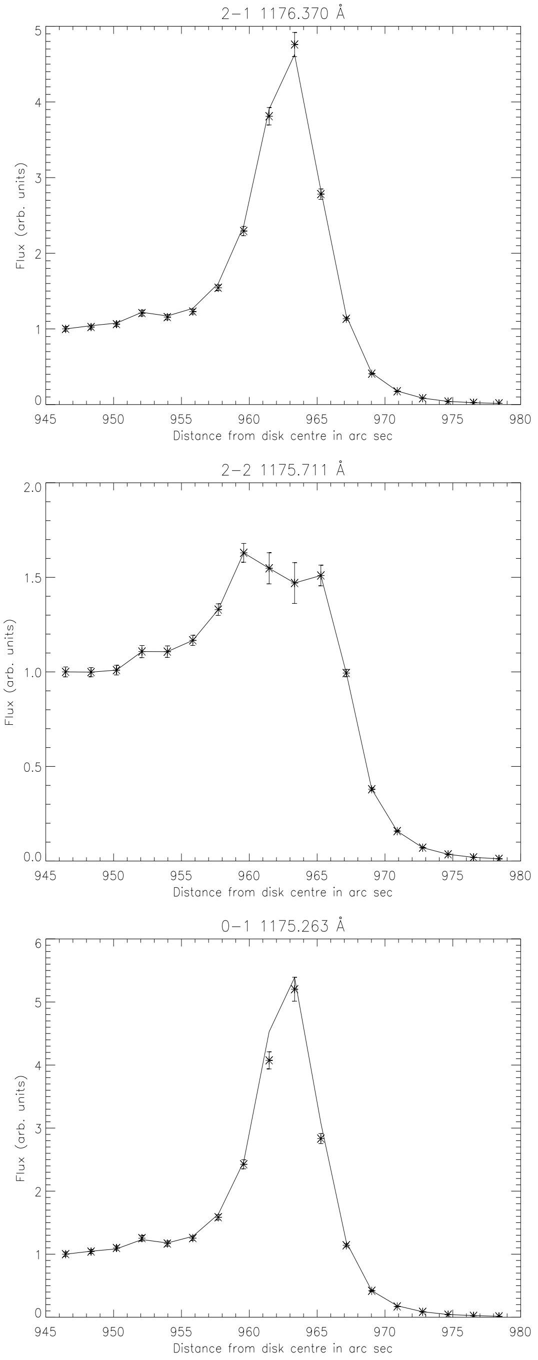

Figure 6.8: Observed fluxes versus raster position for each component of the C III $2s2p\ ^3P - 2p^2\ ^3P$ multiplet. Overlaid are plots of $f_{los}\{\tau_0\}\tau_0\bar{g}^{(i)}\{\tau_0\}$ where the optical depths are those deduced from the observed branching ratios which are listed for the 2–2 component in table 6.1. The factors $f_{los}\{\tau_0\}$ are determined such that the observed and predicted fluxes in fig. 6.7 match exactly.

thus also the greatest degree of blending. Furthermore the discrepancy is most marked for the 1–1 line which is in turn the most significantly blended of the two. These facts suggest that the discrepancies in the 1–1 and 1–0 components relate to the difficulty in resolving these lines and not due a weakness in the escape probability analysis. It is also true that the 1–1 and 1–0 components are the most optically thin of the multiplet (see table 2.7) which might suggest that the discrepancies in these lines are due to a dependence of $f_{los}\{\tau_0\}$ on optical depth. However, the 1–0 component has a comparable optical depth to that of the 0–1 component which shows good agreement between predicted and observed intensities.

Fig. 6.9 shows the same as fig. 6.8 but for the components of the C II $2s^2 2p\ ^2P$ – $2s2p^2\ ^2P$ multiplet. In these plots there is good agreement between model and observed fluxes for all the components with the only exception being the 1/2–1/2 component which is *not* the most optically thin. In fact it is the closest in optical depth to the *control* line (i.e. the one that determines the $f_{los}\{\tau_0\}$ values). It is, however, the most severely blended of all the lines of this multiplet.

Fig. 6.10 shows observed fluxes versus raster position for each component of the C II $2s^2 2p\ ^2P$ – $2s2p^2\ ^2P$ multiplet at ∼ 1036 Å again with plots of $f_{los}\{\tau_0\}\tau_0\bar{g}^{(i)}\{\tau_0\}$ overlaid. Here there is near perfect agreement between the two lines, neither of which are blended.

It follows then that $f_{los}\{\tau_0\}$ is independent of optical depth, τ_0, since the same set of factors, $f_{los}\{\tau_0\}$, are effective for each line even though the optical depth varies from line to line. Further confirmation of this follows from the findings of secs 6.3.1 and 6.3.2 in which it was found that at the limb the stratified models, coupled with the escape probability techniques, overestimate both the emergent fluxes and the C III branching ratios at the limb. Furthermore, at heights above ∼ 970 arc sec both the C II and C III emergent fluxes are underestimated whereas the branching ratios are overestimated if the effects of instrumentally scattered light are neglected. At the limb the stratified model predicts column densities too great to match the emergent fluxes but too small to match the ratios. This discrepancy is removed if the emitting structures in the vicinity of the limb are partially or wholly unresolved. Well beyond the limb the ratios indicate optical depths comparable with those on

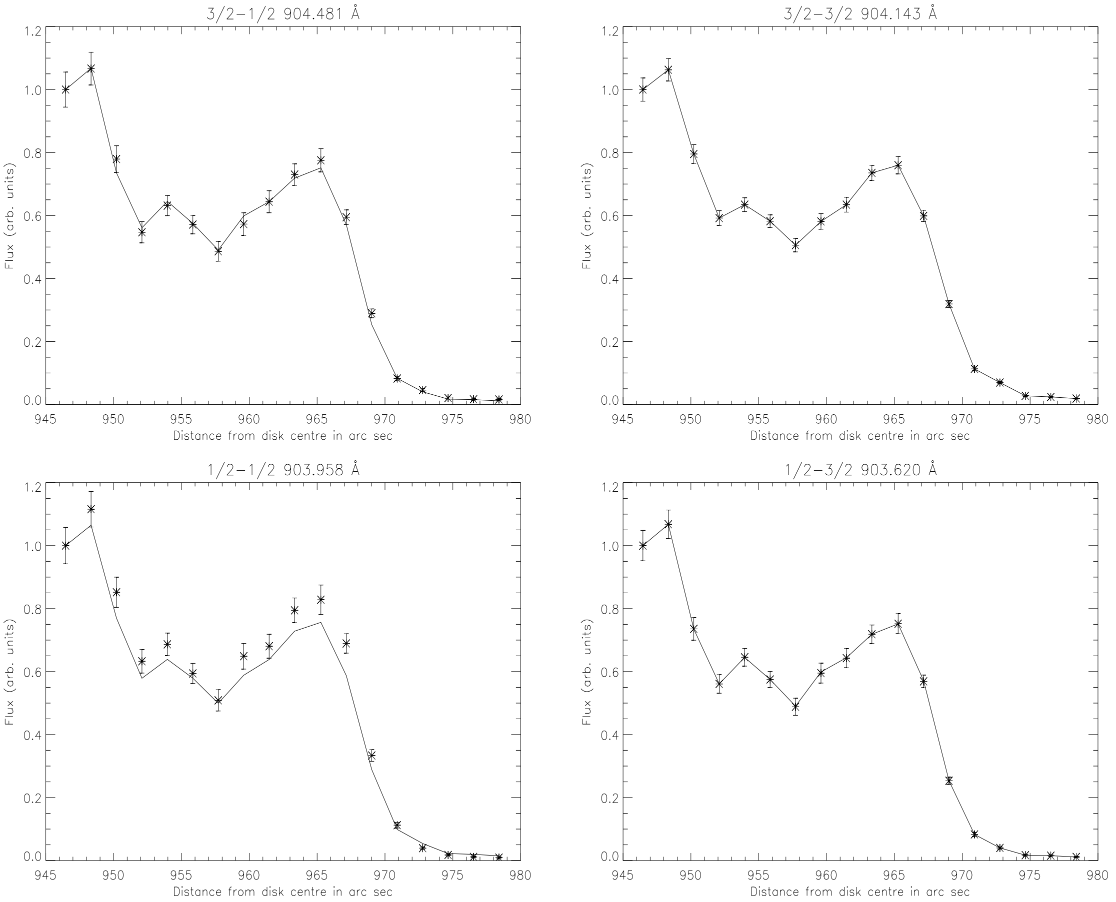

3/2−1/2 904.481 Å

3/2−3/2 904.143 Å

1/2−1/2 903.958 Å

1/2−3/2 903.620 Å

Figure 6.9: Observed fluxes versus raster position for each component of the C II $2s^22p$ ^2P – $2s2p^2$ ^2P multiplet. Overlaid are plots of $f_{los}\{\tau_0\}\tau_0\bar{g}^{(i)}\{\tau_0\}$ where the optical depths are those deduced from the observed branching ratios which are listed for the 3/2–3/2 in table 6.3. The factors $f_{los}\{\tau_0\}$ are determined such that the observed and predicted fluxes for the 3/2–3/2 component match exactly.

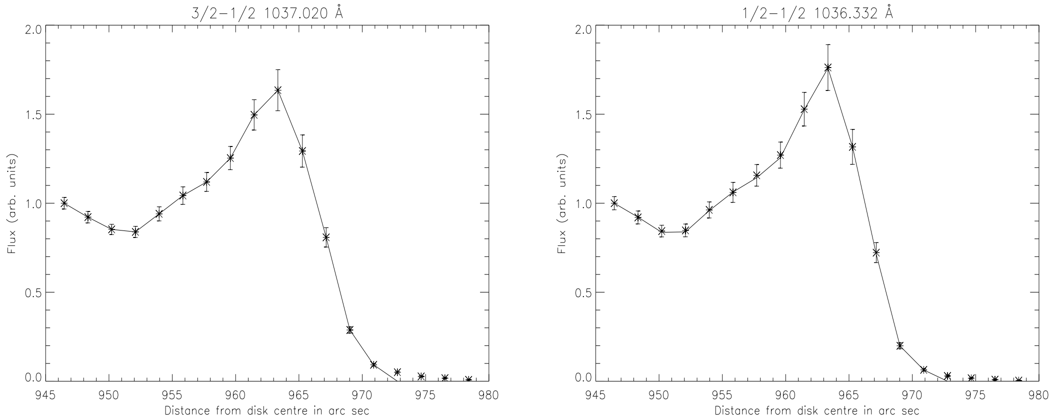

Figure 6.10: Observed fluxes versus raster position for each component of the C II $2s^22p\ ^2P$ – $2s2p^2\ ^2P$ multiplet. Overlaid are plots of $f_{los}\{\tau_0\}\tau_0\bar{g}^{(i)}\{\tau_0\}$ where the optical depths are those deduced from the observed branching ratios which are listed for the 3/2–1/2 in table 6.2. The factors $f_{los}\{\tau_0\}$ are determined such that the observed and predicted fluxes for the 3/2–1/2 component match exactly.

the disk despite the fact that the observed fluxes are significantly lower than those in this region. Moreover, the inclusion of instrumentally scattered light is insufficient to resolve this discrepancy. This signal, being true, again suggests the presence of unresolved structures.

This body of evidence demonstrates that the discrepancy in fig. 6.7 is not due to the spatial variation of the source function but is due to structure. It follows that the neglect of the dependence of the source function on space is appropriate and the line-of-sight averaged escape probability is effective.

6.7 Implications for transition region structure

It has been concluded that $f_{los}\{\tau_0\}$ may be interpreted as a filling factor, which represents the area of the slit occupied by emitting structures. Since it is independent of optical depth, it may be written as f_{los}. The deduced filling factors for the C II multiplets at 904 and 1036 Å are shown in figs 6.11a and b respectively and those of the C III multiplet at 1775 Å are shown in fig. 6.12. In each case the factors are

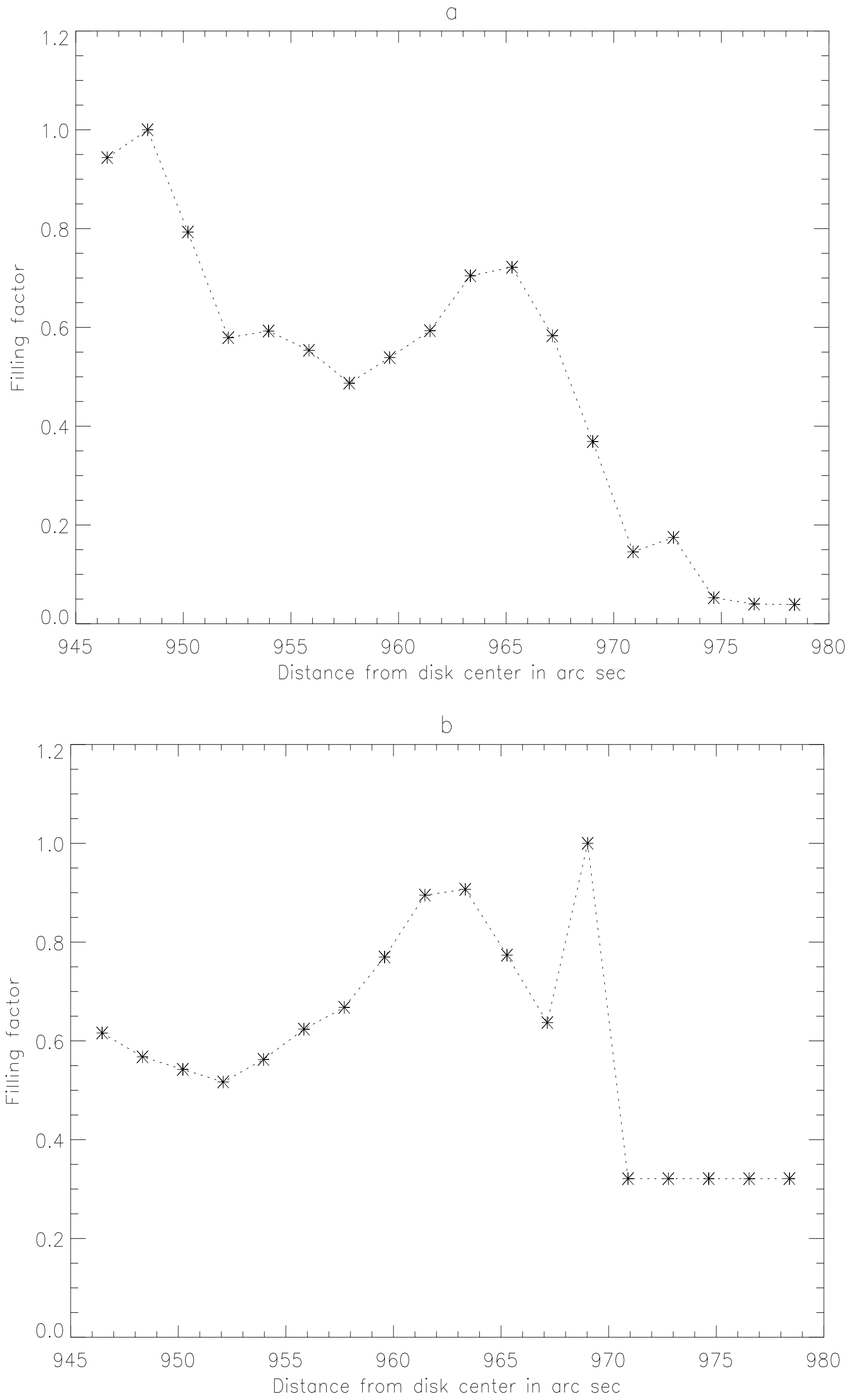

Figure 6.11: C II filling factors (f_{los}) versus pointing position for lines of (a) the 904 Å multiplet and (b) the 1036 Å multiplet. In (b) the filling factor values for the four highest pointing positions set to the value at 970.9 arc sec since no optical depths were deduced for these points (see table 6.2).

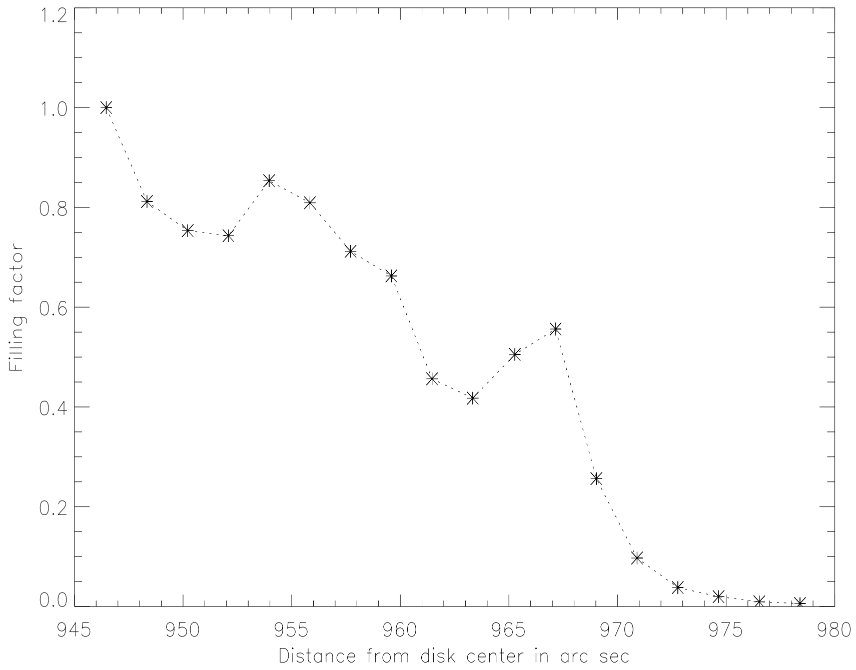

Figure 6.12: C III 1775 Å multiplet filling factors versus pointing position.

scaled to be unity at 946.462 arc sec. There is a general downward trend evident in figs 6.11a and 6.12 indicating a decrease in occupation of the slit by emitting structures with distance from disk centre. No such trend is evident in fig. 6.11b. In each figure, however, strong variations are evident. This variability implies that the absolute filling factors are unity at no more than one pointing position and are thus unlikely be unity anywhere. This implies the presence of unresolved structures at each pointing position – i.e. on the disk, at the limb and beyond.

Of course, the observed fluxes are summed over the slit which has a length of ~ 60 arc sec. Thus the filling factors here correspond to the presence of spicule-like structures of diameter less than 60 arc sec. Such structures are evident in figs 2.8a and b. If at each pointing position the pixels are sorted according to their brightness, then the data may be split into regions associated with resolved structures and regions that are visibly in between the observable structures.

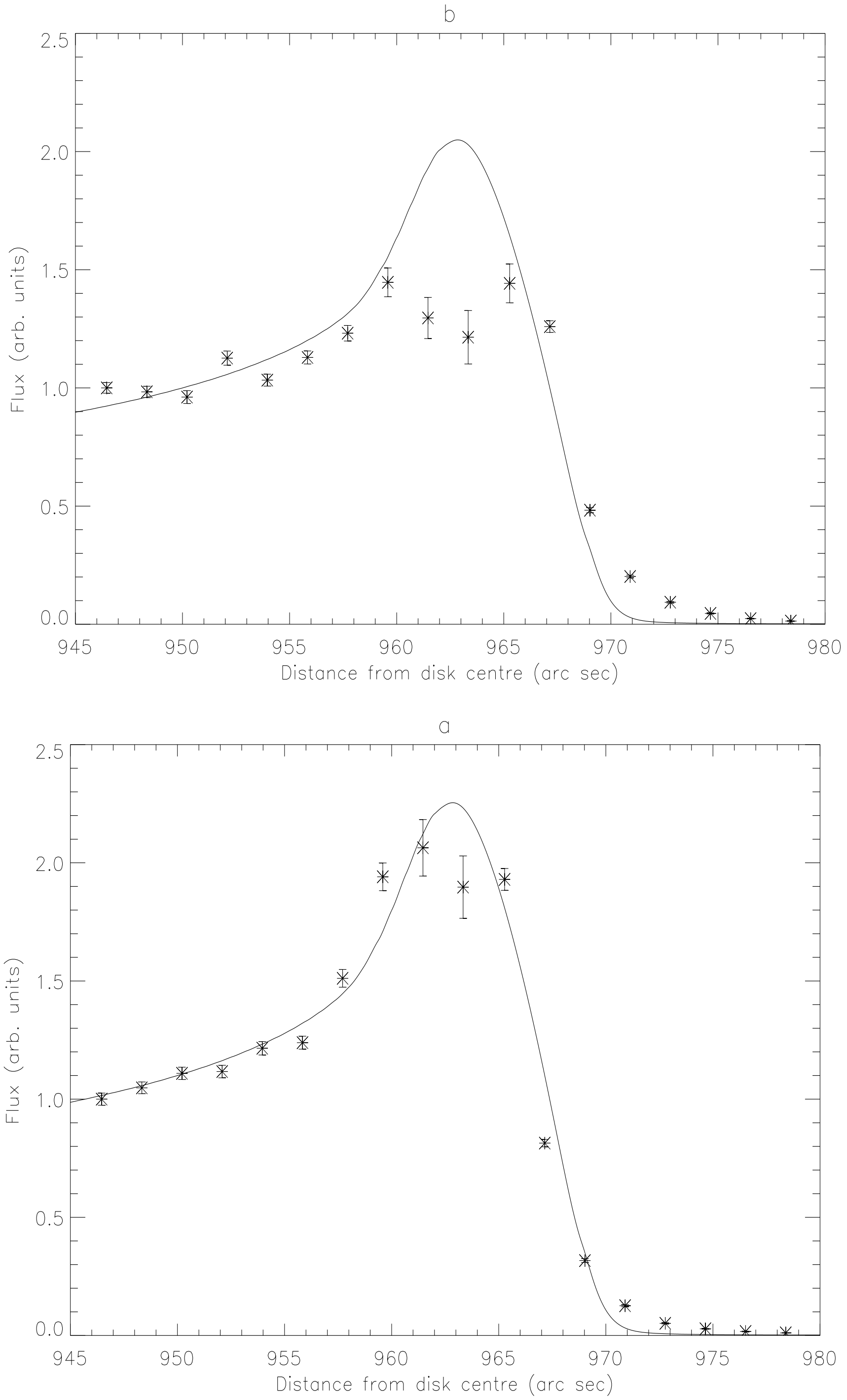

Figure 6.13: Observed fluxes of the C III $2s2p\ ^3P_2 - 2p^2\ ^3P_2$ line at 1175.711 Å compared with predicted values based on an exponential density model overlaid, for (a) regions associated with observable structure and (b) regions not associated with observable structure.

Figs 6.13a and b show observed and model fluxes of the C III $2s2p\ ^3P_2 - 2p^2\ ^3P_2$ line at 1175.711 Å for regions associated and not associated with observable structure. For regions associated with structure the stratified model clearly fails as before. For the *intra-structure* regions, however, the stratified model is much more effective. Figs 6.14a and b, on the other hand, show the same observed fluxes this time in comparison with $\tau_0\bar{g}^{(i)}\{\tau_0\}$. In both cases there is a significant deviation indicating the presence of unresolved structures even in the *intra-structure* data.

6.8 Concluding remarks

In this chapter the C II and C III spectral data discussed in chapter 2 has been reassessed both from a modelling and diagnostic perspective. The stratified models previously considered have been re-applied with an improved calculation of optical depth and with line blending and instrumentally scattered light included. The resultant fits to both observed fluxes and branching ratios are more effective at certain positions and less effective at others as compared with those of chapter 2. Optical depths at disk centre extracted from these models are comparable with those obtained in chapter 2. The deduced density scale height for C II is also comparable with that or chapter 2 but the C III value differs due to a poor fit to the branching ratios of this ion in the vicinity of the limb.

The inclusion of scattered light improves the fit to the branching ratios at positions above $\sim$ 970 arc sec but fails to account for the observed fluxes at such heights. This implies that the observed emission at such heights is not dominated by scattered light which in turn suggests that the emitting structures are observationally unresolved.

Consideration of observed fluxes in comparison with $\tau_0\bar{g}^{(i)}\{\tau_0\}$ confirms the conclusion that the discrepancy between model and observed fluxes is due to the presence of unresolved emitting structures. This analysis serves also to validate the assumption asserted in chapter 3 that the spatial variation of the source function due to the variation of (T_e, N_e) is negligible in this context. This in turn confirms the effectiveness of the line-of-sight averaged escape probability, $\bar{g}^{(i)}\{\tau_0\}$, in a moderate disk centre optical depth regime.

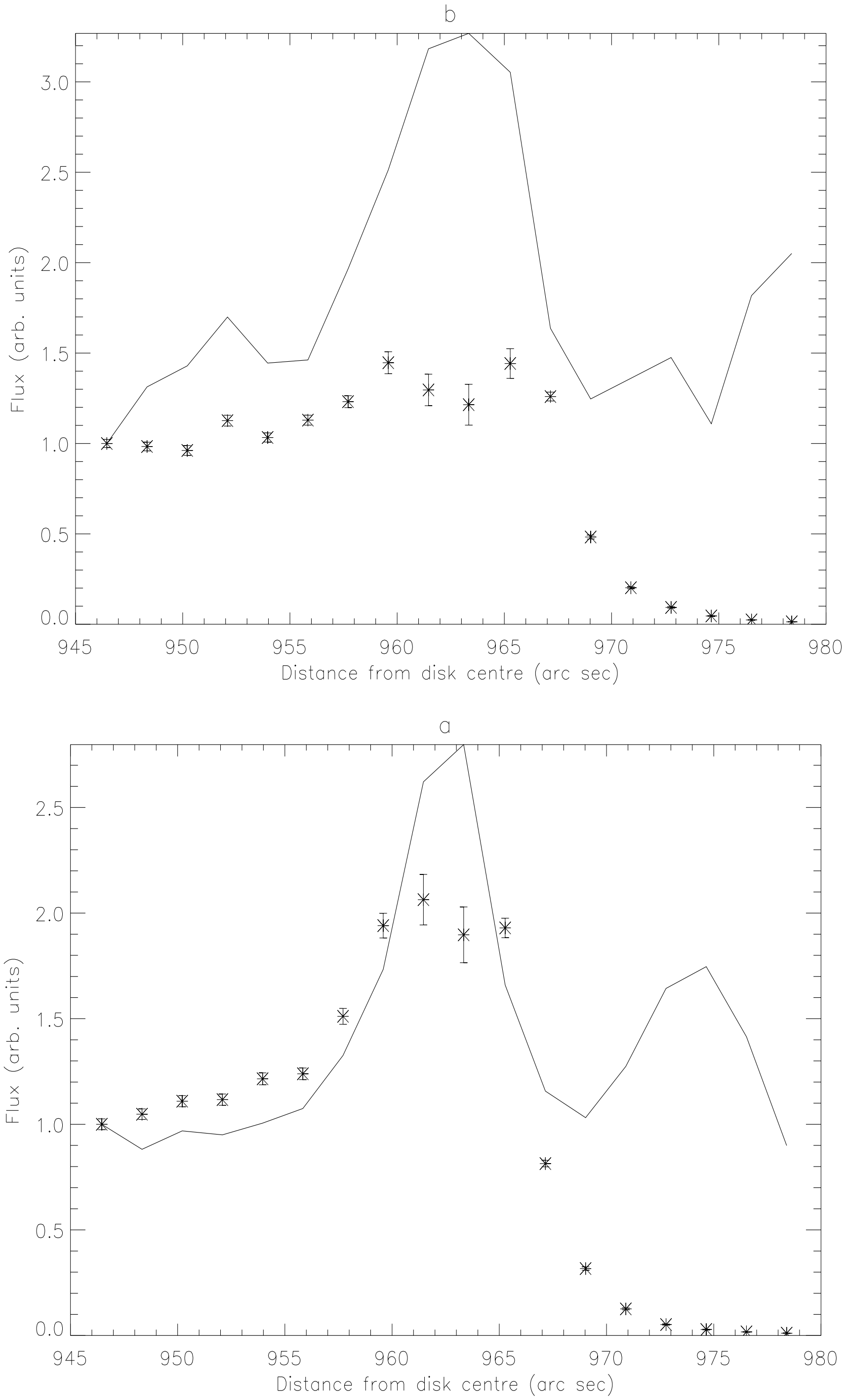

Figure 6.14: Observed fluxes of the C III $2s2p\ {}^3P_2 - 2p^2\ {}^3P_2$ line at 1175.711 Å with $\tau_0 \bar{g}^{(i)}\{\tau_0\}$ overlaid, for (a) regions associated with observable structure and (b) regions not associated with observable structure.

Scaled filling factors, which represent the portion of the slit occupied by emitting structures have been deduced for the 904 Å and 1036 Å multiplets of C II and the 1175.711 Å multiplet of C III. These demonstrate the presence of unresolved emitting structures at positions both on the disk and beyond the limb.

The spectral data has been split into regions visibly associated with and not associated with spicule-like structures. For the *intra-spicule* data the stratified model is effective in describing the observed C III $2s2p\ ^3P_2 - 2p^2\ ^3P_2$ line (1175.711 Å) fluxes. This is not the case for the *spicular* data. For both datasets, however, filling factors may be deduced indicating the presence of unresolved emitting structures within both the *intra-spicule* and *spicule* regions.